

## Acoustic liners and their induced drag

Shahzad, Haris; Hickel, Stefan; Modesti, Davide

**Publication date**

2022

**Document Version**

Final published version

**Citation (APA)**

Shahzad, H., Hickel, S., & Modesti, D. (2022). *Acoustic liners and their induced drag*. Paper presented at 12th International Symposium on Turbulence and Shear Flow Phenomena, TSFP 2022, Osaka, Virtual, Japan.

**Important note**

To cite this publication, please use the final published version (if applicable). Please check the document version above.

**Copyright**

Other than for strictly personal use, it is not permitted to download, forward or distribute the text or part of it, without the consent of the author(s) and/or copyright holder(s), unless the work is under an open content license such as Creative Commons.

**Takedown policy**

Please contact us and provide details if you believe this document breaches copyrights. We will remove access to the work immediately and investigate your claim.

***Green Open Access added to TU Delft Institutional Repository***

***'You share, we take care!' - Taverne project***

**<https://www.openaccess.nl/en/you-share-we-take-care>**

Otherwise as indicated in the copyright section: the publisher is the copyright holder of this work and the author uses the Dutch legislation to make this work public.

## ACOUSTIC LINERS AND THEIR INDUCED DRAG

**Haris Shahzad**

Faculty of Aerospace Engineering  
Delft University of Technology  
Kluyverweg 2, 2629 HS Delft,  
The Netherlands  
h.shahzad@tudelft.nl

**Stefan Hicckel**

Faculty of Aerospace Engineering  
Delft University of Technology  
Kluyverweg 2, 2629 HS Delft,  
The Netherlands  
s.hicckel@tudelft.nl

**Davide Modesti**

Faculty of Aerospace Engineering  
Delft University of Technology  
Kluyverweg 2, 2629 HS Delft,  
The Netherlands  
d.modesti@tudelft.nl

### ABSTRACT

In order to reduce the noise emitted by aircraft engines, the nacelle is coated with acoustic liners. An undesirable effect of these surfaces is that they increase the aerodynamic drag. In the present work, we characterize this type of surface roughness by performing Direct Numerical Simulations of fully resolved acoustic liner geometries. We find evidence of a fully rough regime, whose onset is determined by the value of the viscous-scaled Forchheimer coefficient. Moreover, the intensity of the wall-normal velocity fluctuations at the wall also scales with the viscous-scaled wall-normal permeability, leading to a relation between fluctuations and added drag.

### INTRODUCTION

Aircraft engines are the primary source of noise during take-off and landing. In order to meet the noise regulations, the nacelle of modern engines is coated with acoustic liners, which represent the state-of-the-art technology for engine noise abatement. Acoustic liners are panels with a sandwich structure, consisting of a honeycomb core bounded by a perforated facesheet and a backplate. They typically cover the inner nacelle surface in front of the fan and in the by-pass flow. The working principle of acoustic liners is based on the idea of the Helmholtz resonator, namely a cavity and a throat which dissipates the energy of incoming acoustic waves. An undesirable side effect of these surfaces is that they increase the total aircraft drag, essentially behaving as distributed surface roughness. The acoustic absorption of acoustic liners has been studied extensively as far back as the work of Sivian (1935) and Ingård & Labate (1950), while added drag has been accepted as inevitable. However, moving towards cleaner aviation requires a more in-depth understanding of the drag increase over these surfaces.

Acoustic liners can have a significant effect on the turbulent mean flow as the liner facesheet can not be considered hydraulically smooth. Furthermore, unlike canonical roughness, acoustic liners present a permeable surface to the incoming turbulent flow resulting in a relaxation of the wall-

impermeability. Permeable surfaces have been studied far less than canonical roughness geometries, and it is not clear whether several aspects of rough wall turbulent flow also apply to permeable surfaces. Manes *et al.* (2009) and Breugem *et al.* (2006) studied the differences between permeable surfaces and canonical rough surfaces and showed how permeable surfaces might have a much more profound effect on the flow. Manes *et al.* (2009) further noted that the drag increase over a permeable surface is higher than over a rough surface with the similar geometry. Breugem *et al.* (2006) and Kuwata & Suga (2017) have also noted a breakdown of outer layer similarity over permeable surfaces.

Furthermore, the interaction of a turbulent flow with a permeable surface can change dramatically depending upon the geometry, and unlike canonical (i.e homogeneous) permeable surfaces, acoustic liners have not been studied extensively. Experiments and numerical simulations of the flow over realistic liners are challenging. The diameter of the orifices  $d$  is significant with respect to the boundary layer thickness ( $d/\delta \approx 0.1$ ) and much larger than the viscous length scale ( $d^+ = d/\delta_v \approx 200$ ), where  $\delta$  is the boundary layer thickness and  $\delta_v = \nu_w/u_\tau$  is the viscous length scale based on  $u_\tau = \sqrt{\tau_w/\rho_w}$  where  $\nu_w$ ,  $\rho_w$  and  $\tau_w$  are the wall kinematic viscosity, wall density and the drag per plane area, respectively. Simultaneously satisfying these constraints on the diameter implies high computational cost. Therefore, previous numerical studies have avoided resolving the entire geometry. For instance, Scalo *et al.* (2015) performed Large Eddy Simulation of turbulent channel flow with an impedance boundary condition modelling the liner. They performed simulations at a bulk Reynolds number,  $Re_b = 6900$ , and bulk Mach number,  $M_b = 0.02-0.5$ , and observed a drag increase of up to 350%.

Tam *et al.* (2014) opted for 2D Reynolds Averaged Navier Stokes (RANS) simulations of an array of acoustic liners and estimated a drag increase of about 4% in the presence of 140dB acoustic waves. Zhang & Bodony (2016) aimed at replicating the geometry studied at the Grazing Flow Impedance Tube (GFIT) facility at NASA (Jones *et al.*, 2004) and carried out Direct Numerical Simulation (DNS) of a turbulent boundary

layer over an isolated cavity. Zhang & Bodony (2016) performed DNS at  $Re_\theta = 2300$  and Mach number,  $M = 0.5$ , noting a drag increase of 4.2% without acoustic waves and 25% with 140dB acoustic waves.

The added drag has been extensively documented using experiments at the GFIT (Howerton & Jones, 2015, 2016, 2017) resulting in a large database for acoustic liners geometries and the drag they induce. These studies have helped identify geometrical parameters that can be fine-tuned to reduce acoustic liner drag. The experiments note that the additional drag can be as low as 10% or as high as 350%, depending upon the geometry considered. They further note that small modifications in the geometry can be made without altering acoustic attenuation. Therefore, there is significant room to aerodynamically optimise acoustic liners, which has largely been neglected until now, without compromising on acoustic performance.

Previous studies have attempted to characterise acoustic liner drag. However, numerical studies applied significantly simplifying models, such as the use of modelled boundary conditions and isolated cavities, and experiments are affected by significant uncertainties in the drag measurement and can not provide detailed information about turbulent flow structures. The discrepancies between previous studies is therefore very large and it remains unknown whether acoustic liners behave as canonical roughness or porous surfaces. In this work, we aim to accurately quantify the drag variation induced by acoustic liners in the absence of incoming acoustic waves. We tackle the problem by performing DNS of turbulent channel flow over fully resolved acoustic liner geometries.

## METHODOLOGY

We perform DNS of turbulent channel flow with constant bulk velocity using the solver STREAmS (Bernardini *et al.*, 2021). The channel is a rectangular box of size  $L_x \times L_y \times L_z = 3\delta \times 2\delta \times 1.5\delta$ , where  $\delta$  is the channel half-width. We use a uniform mesh spacing in the streamwise and spanwise directions. In the wall-normal direction, the mesh is clustered towards the wall and coarsened towards the backplate and the channel centre. The simulations are performed at bulk Mach number,  $M_b = u_b/c_w = 0.3$ , where  $u_b$  is the bulk flow velocity and  $c_w$  is the speed of sound at the wall. The upper and lower channel walls are replaced by acoustic liners using a ghost-point immersed boundary method (Vanna *et al.*, 2020).

We choose the liner geometry to match as close as possible the realistic parameters of acoustic liners in operating conditions. Our cavity geometry has a square cross-section with a side length  $\lambda = 0.335\delta$ , depth,  $k = 0.5\delta$ , and the orifices have a diameter  $d = 0.08\delta$ , where  $\delta$  is the channel half-width. The computational domain comprises a total of 64 cavities: an array of  $8 \times 4$  in the streamwise and spanwise direction, respectively, covering both upper and lower walls of the channel. We vary the liner porosity (i.e. open area ratio), between  $\sigma = 0.03$ – $0.32$  by varying the number of orifices per cavity between 1 and 9, while keeping fixed the friction Reynolds number  $Re_\tau = \delta/\delta_v = 500$ . Additionally, we carry out simulations at fixed porosity  $\sigma = 0.32$ , and increase the friction Reynolds number to  $Re_\tau = 1000$  and  $2000$ . This corresponds to a viscous-scaled orifice diameter ranging between  $d^+ = 40$  –  $160$ . Details of the flow cases are shown in Table 1. The orifice configurations within a cavity, along with an instantaneous flow visualisation of the flow field for  $\sigma = 0.32$  and  $Re_\tau = 2000$ , are shown in Figure 1, where vortical structures are visualised using the Q-Criterion. The figure also

shows the top view of a single cavity and the distribution of the orifices. We compare the results of the liner simulations with smooth-wall simulations at approximately matching friction Reynolds number. Quantities that are non-dimensionalised by  $\delta_v$  and  $u_\tau$  are denoted by the ‘+’ superscript.

## RESULTS

### Mean Velocity Profile and Drag Increase

Figure 2 shows the mean velocity profiles for all flow cases, where  $\tilde{\cdot}$  is the Favre averaging operator. Liner cases show a downward shift of the viscous-scaled mean velocity profile with respect to the smooth-wall,  $\Delta U^+$  in the logarithmic region, which is a clear symptom of drag increase. The flow case with low porosity,  $\sigma = 0.0357$  and  $d^+ = 40$  (circles), shows a smooth-wall-like behaviour with minor changes in the velocity profile. However, differences from the smooth-wall velocity profile become evident as either  $\sigma$  or  $d^+$  is increased. The effect of the liner is restricted to the near-wall region, and velocity profiles are parallel to those obtained with a smooth wall in the logarithmic and in the outer layer, supporting Townsend’s outer layer similarity hypothesis.

A fundamental question is whether acoustic liners behave as canonical roughness, that is, whether the Hama roughness function can characterise the drag increase,  $\Delta U^+ = \kappa^{-1} \log(\ell^+) + B(\ell^+)$ , where  $\kappa = 0.4$  is the von Kármán constant, and  $\ell$  is a suitable roughness length scale. In canonical k-type roughness,  $\ell$  is simply the roughness height. However, for acoustic liners, different choices are possible. We consider first the orifice diameter. Figure 2(a) shows  $\Delta U^+$  evaluated at  $y^+ \approx 100$  as a function of  $d^+$ . The figure shows that  $d^+$  is not a suitable length scale because  $\Delta U^+$  increases for a constant  $d^+$  as the porosity increases. The drag increase is, therefore, not only a function of the viscous-scaled orifice diameter, motivating the use of the permeability as a possible parameter for acoustic liners. The permeability represents the ease with which fluid passes through a porous surface and incorporates the effects of changes to the diameter and the porosity into a single variable. We consider the square root of the viscous-scaled wall-normal Darcy permeability  $\sqrt{K^+}$  and the inverse of the wall-normal Forchheimer coefficient,  $1/\alpha^+$ , also referred to as non-linear permeability. The Darcy coefficient represents the pressure drop through a permeable surface within the limit of Stokes flow, and the Forchheimer coefficient is relevant if the inertial effects are more significant. Figure 3 shows  $\Delta U^+$  as a function of the square root of the wall-normal permeability and the Forchheimer coefficient. The former does not lead to a monotonic curve and is, therefore, also not a suitable parameter. Instead, we find that the inverse of the wall-normal Forchheimer coefficient,  $1/\alpha$ , is more appropriate for characterising the additional drag. We see that by increasing  $1/\alpha^+$ ,  $\Delta U^+$  tends towards  $\kappa^{-1} \log(1/\alpha^+) - 3.5$ , suggesting the existence of a fully rough regime. Such a trend suggests that the ease with which the momentum transfer occurs between the two regions of the flow, above and below the facesheet, is dominated by inertial effects.

Further evidence that the inverse of the Forchheimer coefficient is the defining length scale for acoustic liner behaviour is that essentially no change in  $\Delta U^+$  is observed if the spacing of the holes is modified. The Darcy and Forchheimer coefficients are geometrical parameters of a particular geometry and depend primarily on the porosity  $\sigma$  and the thickness to diameter ratio  $t/d$  (Bae & Kim, 2016). Therefore, changing the distribution of the holes does not change the permeability coefficients, as observed by Bae & Kim (2016). Case  $L_{u4}$  has

	$Re_b$	$Re_\tau$	$d^+$	$\sigma$	$\sqrt{K}^+$	$1/\alpha^+$	$\Delta U^+$	$\Delta x^+$	$\Delta y_{min}^+$	$\Delta y_{max}^+$	$\Delta z^+$
$S_1$	9268	506.1	0	0	0	0	-	5.1	0.80	3.83	5.1
$S_2$	21180	1048	0	0	0	0	-	5.2	0.80	4.45	5.2
$S_3$	45240	2060	0	0	0	0	-	5.2	0.80	6.67	5.2
$L_1$	9139	503.5	40.3	0.0357	1.04	0.0528	0.14	1.1	0.80	5.81	1.1
$L_2$	8794	496.4	39.7	0.142	2.06	0.859	0.56	1.0	0.80	5.81	1.0
$L_3$	8264	505.3	40.4	0.322	3.22	5.14	1.90	1.0	0.81	5.81	1.0
$L_4$	19505	1038	83.0	0.142	4.30	1.718	0.96	2.1	0.83	6.30	2.1
$L_{u4}$	19505	1044	83.5	0.142	4.32	1.727	0.98	5.9	0.84	6.10	5.9
$L_5$	17810	1026	82.1	0.322	6.53	10.4	2.78	2.1	0.82	6.29	2.1
$L_6$	35470	2044	164.0	0.322	13.0	20.8	4.44	4.1	0.82	6.70	4.1

Table 1. DNS dataset comprising smooth, ( $S_n$ ) and liner ( $L_n$ ) cases.  $\sigma$  is the porosity (open area ratio),  $d^+$  is the orifice diameter,  $K_y$  is the Darcy permeability,  $\alpha$  is the Forchheimer coefficient, and  $\Delta U^+$  is the Hama roughness function. Simulations are performed in computational a box with dimensions  $L_x \times L_y \times L_z = 3\delta \times 3\delta \times 1.5\delta$ .  $\Delta x^+$  and  $\Delta z^+$  are the viscous-scaled mesh spacing in the streamwise and spanwise direction.  $\Delta y_{min}^+$  and  $\Delta y_{max}^+$  are the minimum and the maximum mesh spacing in the wall-normal direction. Liner cases ( $L_1$ )–( $L_6$ ) have equispaced orifices in the streamwise and spanwise direction. Case  $L_{u4}$  has the same porosity and orifice size of  $L_4$ , but the holes are not equispaced in the streamwise direction, see bottom right configuration of Figure 1.

the same porosity and diameter as case  $L_4$  but the orifices are not equispaced in the streamwise direction. However, approximately the same  $\Delta U^+$  is observed. Acoustic liners, therefore, act as a permeable substrate.

### Reynolds Stresses

The effect of the liner can also be seen in the Reynolds Stresses,  $\tau_{ij} = \overline{\rho u_i' u_j'}$ , shown in Figure 4 for liner cases  $L_5$  and  $L_6$ , compared to their respective smooth wall cases, where the double prime symbol indicates fluctuations with respect to the Favre average and  $\overline{\cdot}$  is the Reynolds averaging operator. Significant changes in velocity fluctuations are seen only close to the wall, where non-zero turbulence intensities are observed. An increase in the maximum  $\tau_{33}$  is observed in the presence of the liner, whereas the maximum  $\tau_{11}$  tends to decrease compared to the smooth wall. The maxima of the velocity fluctuations move slightly closer to the wall, irrespective of the component. Together with the non-zero intensity at the wall, enhance momentum transfer near the wall. The total drag increases because of the higher Reynolds stresses and the adverse pressure gradient experienced by the flow at the downstream lip of each orifice. Much smaller differences can be seen in the outer layer. These differences are more pronounced for flow case  $L_6$  with  $1/\alpha^+ \approx 20.8$  and not as noticeable for flow case  $L_5$  with  $1/\alpha^+ \approx 10.4$  suggesting a departure from Townsend's outer layer similarity hypothesis as the inverse of the Forchheimer coefficient is increased.

The trend of the velocity fluctuations is in line with previous research on rough (Endrikat *et al.*, 2021) and permeable walls (Kuwata & Suga, 2016) on turbulent flow. For permeable walls, the wall-normal velocity fluctuations at the wall increase because of a relaxation of the wall blockage effect (Kuwata & Suga, 2019). The reduction in the peak of the streamwise Reynolds Stress results from these high-wall normal velocity fluctuations perturbing the classical near-wall turbulence cycle. High-speed and low-speed streaks, typical of near-wall turbulence, are perturbed by the significant wall-normal velocity fluctuations at the wall and, thus, might break down over

permeable walls (Kuwata & Suga, 2019). The liner induces a similar effect on the turbulent flow. As shown in Figure 5 (a), which shows the velocity fluctuations with respect to the Reynolds average, streaks become shorter over the liner. Even in the liner's presence, the streaky structures can still be discerned, suggesting a modulation rather than a complete replacement of the near-wall cycle.

### Acoustic Liners as Porous Surfaces

Although the trend of the Reynolds stresses is similar to trends observed for permeable surfaces, acoustic liners are different from most canonical porous surfaces. Unlike canonical porous surfaces, the cavity walls prevent a net flow underneath the surface of the facesheet as there is no streamwise and spanwise permeability for acoustic liners. This can lead to significantly altered flow physics. For instance, Kuwata & Suga (2017) performed DNS over permeable surfaces with anisotropic permeability and noted spanwise invariant Kelvin–Helmholtz-like rollers as the streamwise and spanwise permeability is relaxed. No such rollers are observed for the current simulations, possibly because of the geometrical differences between acoustic liners and canonical porous surfaces.

Furthermore, we show supporting evidence that the Forchheimer coefficient is the relevant length scale for the flow in contrast to previous studies of turbulence over canonical porous surfaces (Gómez-de Segura & García-Mayoral, 2020; Rosti *et al.*, 2015) that highlight the importance of the Darcy coefficient. Canonical porous surfaces may exhibit Darcian velocities inside their pores. However, as acoustic liners are large with respect to the viscous length scale, inertial effects are significant inside the orifices of an acoustic liner. Based on our DNS results, we believe that the Forchheimer drag might become the dominant drag on canonical porous surfaces for sufficiently high Reynolds numbers.

Figure 5 (b) shows the wall-normal velocity in a wall-normal plane, where we observe that the effect of the liner on the flow is concentrated near the wall and inside the orifices. Inside the orifices, high wall-normal velocity fluctuations are

visible, and they are notably higher at the downstream edge. A jet-like flow is observed inside the cavities due to the high wall-normal velocity fluctuations, indicating important inertial effects inside the orifices.

Figure 6 (a) shows the intrinsic average of the wall-normal velocity fluctuations for flow case  $L_6$  with  $1/\alpha^+ \approx 20.8$ . High wall-normal velocity fluctuations are observed and are responsible for momentum exchange between the outer flow and flow inside the liner, enhancing mixing and increasing drag. This is in line with prior work, where high values of the wall-normal velocity fluctuations have been often related to drag increase, both over roughness (Orlandi & Leonardi, 2006) and permeable surfaces (Wilkinson, 1983). Wilkinson (1983) focuses on acoustic liner geometries and proposes this blowing and suction effect as one of the possible mechanisms of the drag increase.

For this reason, we report the mean wall-normal velocity fluctuations at the wall as a function of permeability coefficients. Very similar to the trend observed for  $\Delta U^+$ , the maximum average wall-normal velocity does not show a monotonic trend with the  $\sqrt{K^+}$ . In comparison, an almost linear trend is observed with  $1/\alpha^+$  for the wall-normal velocity - suggesting a correlation of the  $\Delta U^+$  with the wall-normal velocity fluctuations similar to the findings of Orlandi & Leonardi (2006) and Wilkinson (1983).

## CONCLUSION AND FUTURE WORK

We performed unprecedented DNS of turbulent flow over fully resolved acoustic liner geometries to study their effect on turbulence and added drag. The parametric study comprises liner porosities in the range  $\sigma = 0.0357 - 0.322$  and viscous-scaled orifice diameters in the range  $d^+ = 40 - 160$ . Our results show that the inverse of the viscous-scaled Forchheimer coefficient is the relevant length scale for the added drag of these surfaces, suggesting that acoustic liners can be regarded as a permeable substrate, within which inertial effects are significant. Our DNS data further supports the existence of a fully rough regime, although simulations at higher  $1/\alpha^+$  would be required to fully confirm this trend.

## ACKNOWLEDGEMENTS

We acknowledge PRACE for awarding us access to Piz Daint, at the Swiss National Supercomputing Centre (CSCS), Switzerland.

## REFERENCES

- Bae, Y. & Kim, Y. I. 2016 Numerical modeling of anisotropic drag for a perforated plate with cylindrical holes. *Chem. Eng. Sci.* **149**, 78–87.
- Bernardini, Matteo, Modesti, Davide, Salvatore, Francesco & Pirozzoli, Sergio 2021 STREAmS: a high-fidelity accelerated solver for direct numerical simulation of compressible turbulent flows. *Comput. Phys. Commun.* **263**, 107906.
- Breugem, W. P., Boersma, B. J. & Uittenbogaard, R. E. 2006 The influence of wall permeability on turbulent channel flow. *J. Fluid Mech.* **562**, 35–72.
- Endrikat, S., Modesti, D., García-Mayoral, R., Hutchins, N. & Chung, D. 2021 Influence of riblet shapes on the occurrence of Kelvin–Helmholtz rollers. *J. Fluid Mech.* **913**.
- Howerton, B. M. & Jones, M. G. 2015 Acoustic Liner Drag: A Parametric Study of Conventional Configurations. In *AIAA paper 2015-2230*.
- Howerton, B. M. & Jones, M. G. 2016 Acoustic Liner Drag: Measurements on Novel Facesheet Perforate Geometries. In *AIAA paper 2016-2979*.
- Howerton, B. M. & Jones, M. G. 2017 A Conventional Liner Acoustic/Drag Interaction Benchmark Database. In *AIAA paper 2017-4190*.
- Ingård, U. & Labate, S. 1950 Acoustic Circulation Effects and the Nonlinear Impedance of Orifices. *J. Acoust. Soc. Am.* **22** (2), 211–218.
- Jones, M., Watson, W. R., Parrott, T. & Smith, C. 2004 Design and Evaluation of Modifications to the NASA Langley Flow Impedance Tube. In *AIAA paper 2004-2837*.
- Kuwata, Y. & Suga, K. 2016 Lattice Boltzmann direct numerical simulation of interface turbulence over porous and rough walls. *Int. J. Heat Fluid Flow* **61**, 145–157.
- Kuwata, Y. & Suga, K. 2017 Direct numerical simulation of turbulence over anisotropic porous media. *J. Fluid Mech.* **831**, 41–71.
- Kuwata, Y. & Suga, K. 2019 Extensive investigation of the influence of wall permeability on turbulence. *Int. J. Heat Fluid Flow* **80**, 108465.
- Manes, C., Pokrajac, D., McEwan, I. & Nikora, V. 2009 Turbulence structure of open channel flows over permeable and impermeable beds: A comparative study. *Phys. Fluids* **21** (12), 125109.
- Orlandi, P. & Leonardi, S. 2006 DNS of turbulent channel flows with two- and three-dimensional roughness. *J. Turbul.* **7**, N73.
- Rosti, Marco E., Cortelezzi, Luca & Quadrio, Maurizio 2015 Direct numerical simulation of turbulent channel flow over porous walls. *J. Fluid Mech.* **784**, 396–442.
- Scalo, C., Bodart, J. & Lele, S. K. 2015 Compressible turbulent channel flow with impedance boundary conditions. *Phys. Fluids* **27** (3), 035107.
- Gómez-de Segura, Garazi & García-Mayoral, Ricardo 2020 Imposing virtual origins on the velocity components in direct numerical simulations. *Int. J. Heat Fluid Flow* **86**, 108675.
- Sivian, L. J. 1935 Acoustic Impedance of Small Orifices. *J. Acoust. Soc.* **7** (2), 94–101.
- Tam, C. K. W., Pastouchenko, N. N., Jones, M. G. & Watson, W. R. 2014 Experimental validation of numerical simulations for an acoustic liner in grazing flow: Self-noise and added drag. *J. Sound Vib.* **333** (13), 2831–2854.
- Vanna, F. D., Picano, F. & Benini, E. 2020 A sharp-interface immersed boundary method for moving objects in compressible viscous flows. *Comput. Fluids* **201**, 104415.
- Wilkinson, S. 1983 Influence of wall permeability on turbulent boundary-layer properties. In *AIAA paper 1983-294*. Reno, NV, U.S.A.
- Zhang, Q. & Bodony, D. J. 2016 Numerical investigation of a honeycomb liner grazed by laminar and turbulent boundary layers. *J. Fluid Mech.* **792**, 936–980.

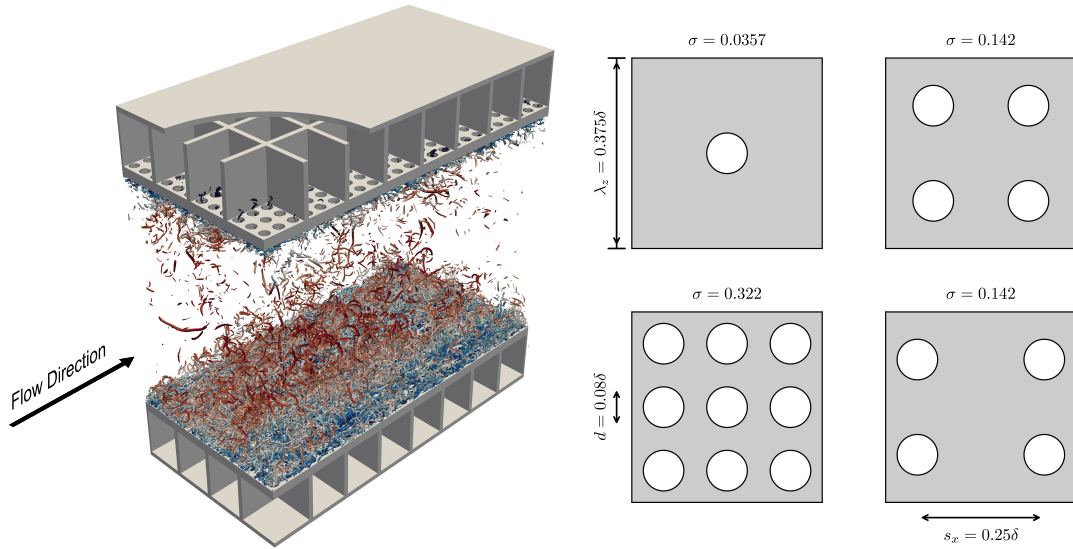


Figure 1. Instantaneous flow field from DNS of turbulent channel flow at  $Re_\tau = 2000$  and bulk Mach number  $M_b = 0.3$ . Vortical structures are visualised using the Q-Criterion. The orifice configurations for the three porosities,  $\sigma$ , studied are shown on the right.

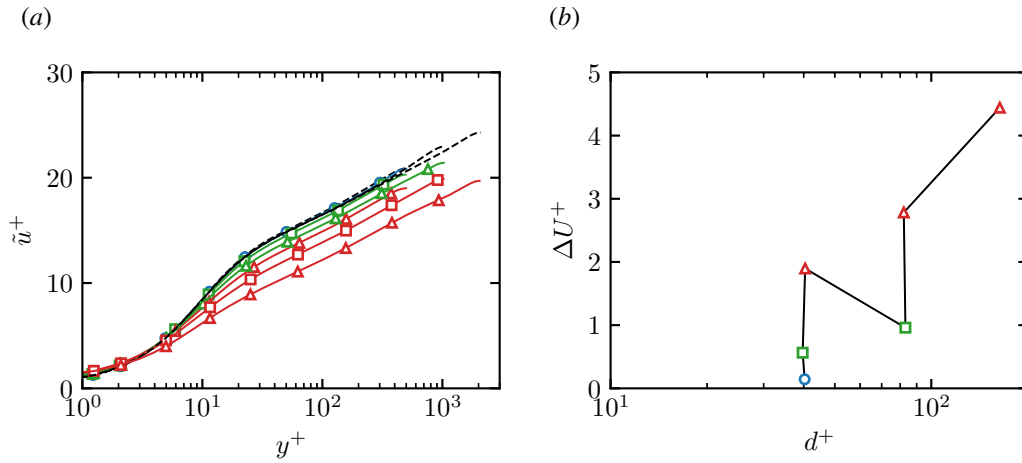


Figure 2. Mean streamwise velocity as a function of the wall-normal distance (a) and  $\Delta U^+$  as a function of the viscous-scaled orifice diameter (b). Symbols indicate different porosities:  $\sigma = 0.0357$  (circles),  $\sigma = 0.143$  (squares) and  $\sigma = 0.322$  (triangles). The dashed line in (a) indicates smooth wall streamwise velocity profiles.

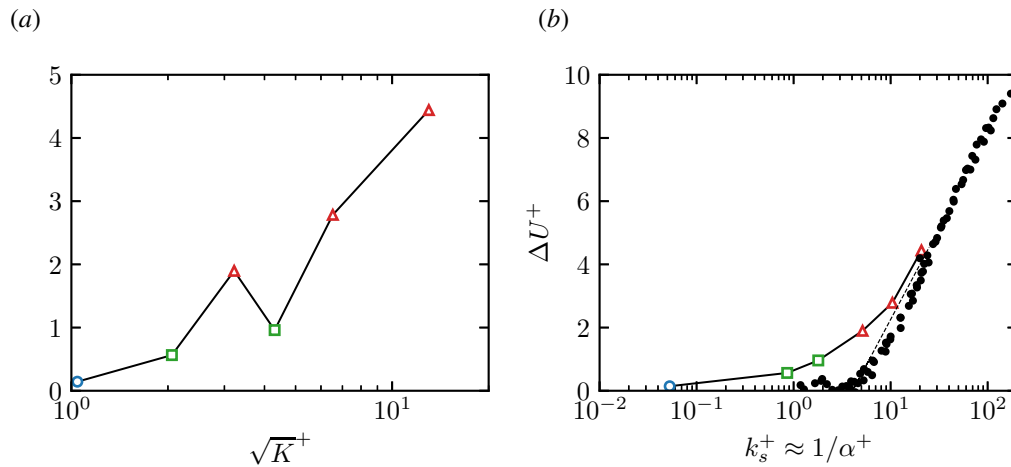


Figure 3.  $\Delta U^+$  as a function of the square root of the Darcy Coefficient (a) and the inverse of the Forchheimer coefficient (b). The dotted line in (b) indicates  $\Delta U^+ = \kappa^{-1} \log(1/\alpha^+) - 3.5$ . Filled circles in (b) represent Nikuradse's data.

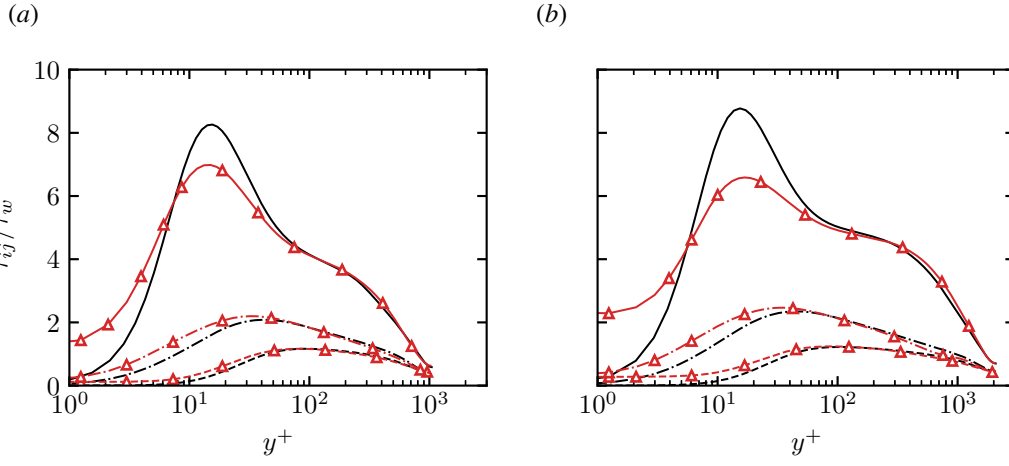


Figure 4. Reynolds stresses as a function of the viscous-scaled wall-normal distance for flow case  $L_5$  with  $1/\alpha^+ = 10.4$  (a) and flow case  $L_6$  with  $1/\alpha^+ = 20.8$  (b). Lines indicate the smooth-wall cases and triangles indicate the liner cases. Solid lines indicate  $\tau_{11}/\tau_w$ , dashed lines indicate  $\tau_{22}/\tau_w$  and dashed-dotted lines indicate  $\tau_{33}/\tau_w$ .

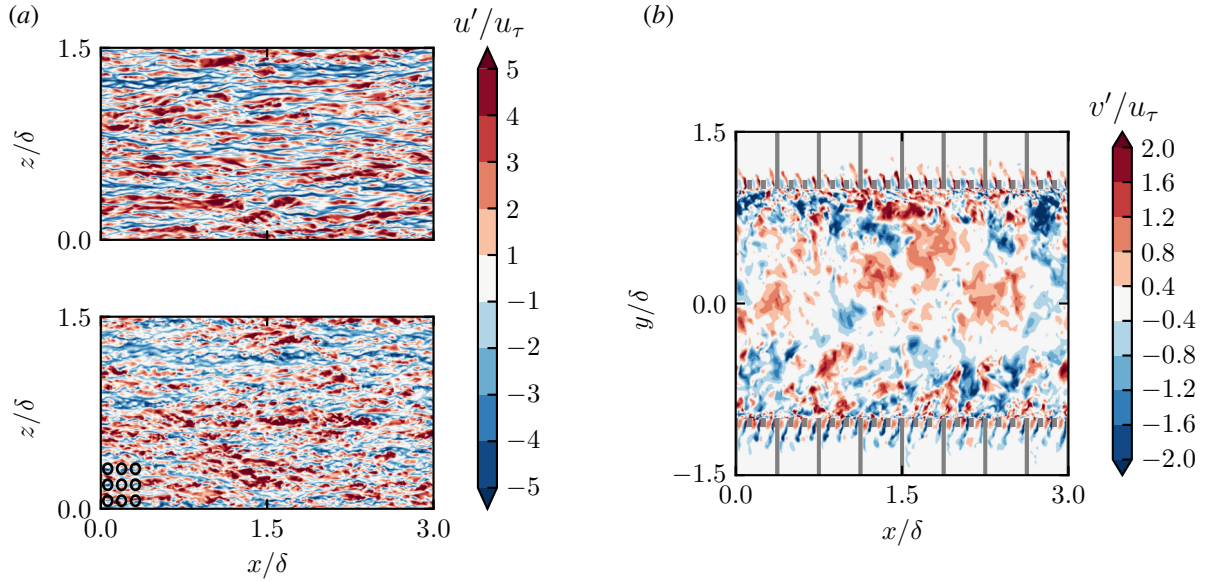


Figure 5. Instantaneous streamwise velocity fluctuations in a wall-parallel plane at  $y^+ = 12$  (a) for flow case  $L_3$  (top) and flow case  $L_6$  (bottom) and instantaneous wall-normal velocity for flow case  $L_6$  (b). In (a), the position of the orifices is shown at the bottom left corner, for one cavity.

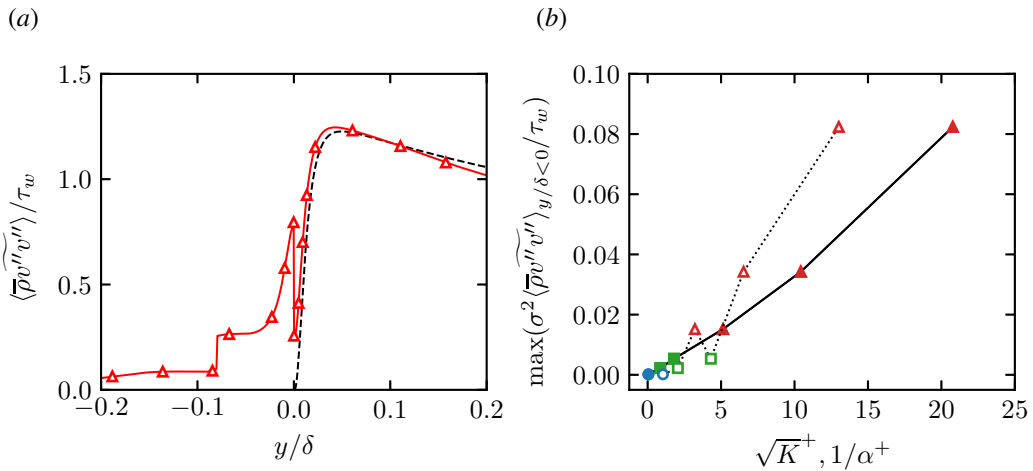


Figure 6. Intrinsic average of the wall-normal velocity fluctuations as a function of the wall distance (a) for flow case  $L_6$  and maximum of the wall-normal velocity fluctuations below the wall (b) as a function of  $1/\alpha^+$  (solid line with filled symbols) and  $\sqrt{K}^+$  (dotted line with empty symbols). The dashed line in (a) indicates the smooth-wall case.